ChemPubSoc Europe

DOI: 10.1002/celc.201801220

CHEMELECTROCHEM Articles

# Minimization of Catalyst Loading on Regenerative Fuel Cell Positive Electrodes Based on Titanium Felts using Atomic Layer Deposition

Stefanie Schlicht,[a] Maïssa K. S. Barr,[a] Mingjian Wu,[c] Paula Hoppe,[d] Erdmann Spiecker,[c] Wolfgang Peukert,[d] and Julien Bachmann*[a, b]

We present the preparation and electrochemical analysis of a novel type of positive regenerative fuel cell electrode based on commercially available Ti felts with a Pt/Ir catalyst. Anodic oxidation of the Ti felts leads to the formation of a $TiO_2$ nanotube layer. The high specific surface area allows for a particularly efficient utilization of the noble metal catalyst. Its loading in the nanoporous system is controlled accurately and minimized systematically by atomic layer deposition. The electrochemical activity towards water splitting of both metals is investigated in acidic media by cyclic voltammetry and steady-state electrolysis for various catalyst loadings. An optimal oxygen evolution reaction is found for a catalyst loading of 76 $\mu g\,cm^{-2}$ resulting in a mass activity of 345 $A\,g^{-1}$ at $\eta = 0.47$ V, whereas the simultaneous presence of Pt at the surface is demonstrated by X-ray photoelectron spectroscopy and by the high activity observed for the hydrogen evolution reaction.

## 1. Introduction

In recent years the contribution of renewable energy sources such as wind and solar as an alternative to fossil fuels has gained in importance. This increase in the contribution of inherently intermittent inputs to the energy grid highlights the importance of energy storage systems needed to ensure a reliable continuous supply. In addition to physical storage devices such as capacitors (for short-term storage) and hydro-electric power plants (for the longer term), the most popular storage systems are batteries (of the lithium-ion type or based on more conventional chemistries for stationary applications). Although these systems provide high energy densities and high capacity for charging and discharging cycles, the high costs are still the limiting factor.[1] An alternative bases on devices in which energy density and power density can be varied in an independent manner, that is, devices with fuel tanks separated from the sites of electrochemical conversion: most prominently the regenerative fuel cell,[1] but also related systems such as the redox flow batteries.[1] A regenerative fuel cell can both store electrical energy into a fuel and dioxygen upon electrolysis and release it when it performs the reverse reaction. The current densities and reversibilities are always limited by the positive electrode, at which the $H_2O/O_2$ couple is located (oxygen evolution reaction and oxygen reduction reaction, or OER and ORR).

State-of-the-art regenerative fuel cells deliver currents on the order of 200–500 $mA\,cm^{-2}$ at elevated temperatures (approximately 80 °C), with round-trip energy efficiencies typically between 30% and 60%.[1] On the rate- and efficiency-limiting positive electrode, a mixture of Pt and Ir (partly oxidized) is standard, with loadings between 0.2 and 5 $mg\,cm^{-2}$ (most often between 2 and 4 $mg\,cm^{-2}$).[1] For energy storage and release in stationary applications such as grid stabilization, the most crucial metric is not so much the current (or power) density but rather the energy efficiency, which can also be called reversibility. In that sense, obtaining moderate current densities at very low overpotential ($< 0.2$ V) is more important than extremely high current densities at overpotentials of 0.5 V and more (corresponding to energy efficiencies below 70% per pass for water splitting, or below 50% round-trip). Furthermore, cost and availability considerations dictate that the noble metal loading be minimized. Thus, we will focus here on minimizing the noble metal loading and will consider the mass activity (current per noble metal amount) at low overpotentials as the most significant performance parameter. The goals to be reached by 2020 according to the technical targets defined by the US Department of Energy (DOE) in fuel cell technology are

[a] S. Schlicht, Dr. M. K. S. Barr, Prof. J. Bachmann
Departement of Chemistry and Pharmacy
Friedrich-Alexander University Erlangen-Nürnberg
Egerlandstrasse 3a, 91058 Erlangen, Germany
E-mail: julien.bachmann@fau.de
[b] Prof. J. Bachmann
Institute of Chemistry
Saint-Petersburg State University
Universitetskii pr. 26, 198504 St. Petersburg, Russia
[c] Dr. M. Wu, Prof. E. Spiecker
Institute of Micro- and Nanostructure Research
Friedrich-Alexander University Erlangen-Nürnberg
Cauerstraße 6, 91058 Erlangen, Germany
[d] P. Hoppe, Prof. W. Peukert
Institute of Particle Technology
Friedrich-Alexander University Erlangen-Nürnberg
Cauerstraße 4, 91058 Erlangen, Germany

Supporting information for this article is available on the WWW under https://doi.org/10.1002/celc.201801220

a total noble metal loading of $\leq 0.125\ mg\,cm^{-2}$ and a mass activity of $\geq 0.44\ A\,mg^{-1}$ (at an overpotential of $\eta \leq 0.33$ V).

In this work, we present the preparation of nanostructured, catalyst-coated titanium felt electrodes for the positive half-cell of regenerative fuel cells. The high specific surface area allows us to utilize the noble metal catalyst most efficiently and thereby to minimize its loading. Nanostructuring is achieved by electrochemical oxidation ('anodization') of commercial Ti felts, whereas the Pt/Ir catalyst is distributed in the porous system homogeneously by atomic layer deposition (ALD). We demonstrate that all 2020 DOE targets mentioned above can be not only met but even exceeded for the water oxidation half-reaction. Finally, we demonstrate that both Pt and Ir are present at the surface and electrochemically active.

## 2. Results and Discussion

### 2.1. Preparation and Characterization of Ti Felts

Our starting material is a commercially available, electrically conductive Ti felt as the electrode substrate. In order to increase its surface area, the felt is anodized under +40 V for 2 h in a solution of 0.5 wt% $NH_4F$ in glycerol.[1] This results in the formation of a $TiO_2$ tube layer around each Ti fiber. Figure 1

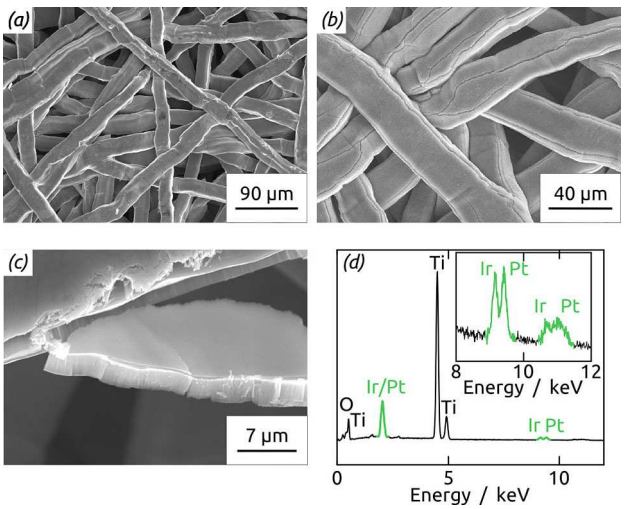


**Figure 1.** Scanning electron micrographs of a Ti felt (a) untreated and (b-c) after anodization in 0.5 wt% $NH_4F$ in glycerol for 2 h. (d) Energy-dispersive X-ray analysis proves the presence of the elements Pt and Ir after atomic layer deposition (expected energies: Ir Lα 9.174 keV, Ir M 1.977 keV, Pt Lα 9.441 keV, Pt M 2.048 keV).

displays the scanning electron micrographs of a Ti felt before and after anodization at different magnifications in top view. The cracks in Figure 1b are associated with the $TiO_2$ layer. An anodization duration of 2 h results in a $TiO_2$ tube length of 2.0 µm, whereas after longer durations the adhesion of the $TiO_2$ becomes poor and it tends to peel off due to the volume expansion generated by the oxidation. (Figure S1 in the Supporting Information)

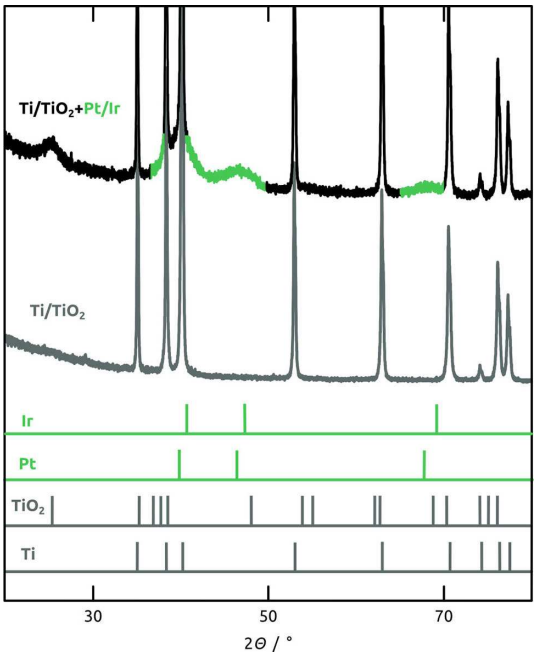


**Figure 2.** X-ray diffraction pattern of an untreated Ti felt, after anodization for 2 h and after ALD coating with platinum/iridium catalyst (highlighted in green).

Subsequently, the Ti felts are coated with platinum and iridium as the bifunctional OER/ORR catalyst by atomic layer deposition (ALD) at 220 °C.[1] ALD provides the experimentalist with the unique ability to coat deep pores in a conformal manner, and an outstanding control of the amount deposited, even at very low loadings.[1]

Energy-dispersive X-ray analysis (EDX, Figure 1d) and X-ray diffraction (XRD, Figure 2) evidence the presence of both elements in crystalline, metallic form after ALD. In EDX, the M lines of Pt and Ir cannot be resolved separately; however, the Lα lines of Pt and Ir are distinct at 9.44 keV and 9.17 keV, respectively. The XRD pattern shows, in addition to the sharp peaks of the Ti substrate, broad signals at $2\theta \approx 40°$ (overlapping with sharper Ti peaks), $\approx 47°$ and $\approx 68°$. These signals are consistent with small particles of intimately mixed Pt/Ir, although the presence of separate Pt and Ir peaks cannot be excluded on the basis of XRD alone due to the similarity of both crystal structures and consequently both patterns (COD 9013417 and COD 9008470).[2] A small anatase peak appears at $\approx 25°$ due to the thermal treatment during ALD deposition at 220 °C (in the absence of thermal treatment, the anodized $TiO_2$ is amorphous). Further information is provided by (scanning) transmission electron microscopic (STEM / TEM) investigation, complemented by EDX elemental mapping and selected-area electron diffraction (SAED).

Figure 3 is an STEM Z-contrast micrograph of a thin area where only one $TiO_2$ tube is revealed along the projection direction (i.e., the projection effect is minimized). The image clearly reveals a well-dispersed layer of particles of diameter $< 5$ nm deposited on the inner surface of the $TiO_2$ tubes. Both metallic elements are present in every particle, and no separate

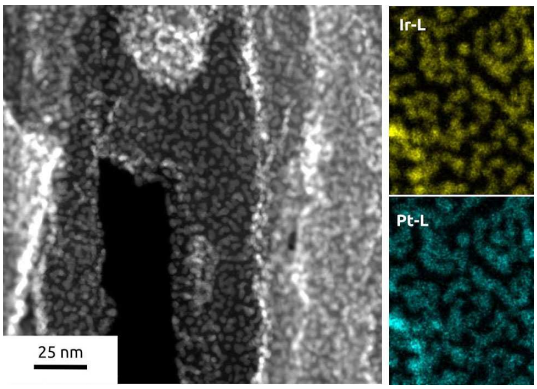


**Figure 3.** High-angle annular dark-field scanning transmission electron microscopy of a lamella lifted out of an anodized Ti felt with Pt/Ir coating. In high magnification, the individual Pt/Ir particles are observable. EDX elemental maps mapping show that the particles are well dispersed along the $TiO_2$ nanotube walls and each contain both Pt and Ir.

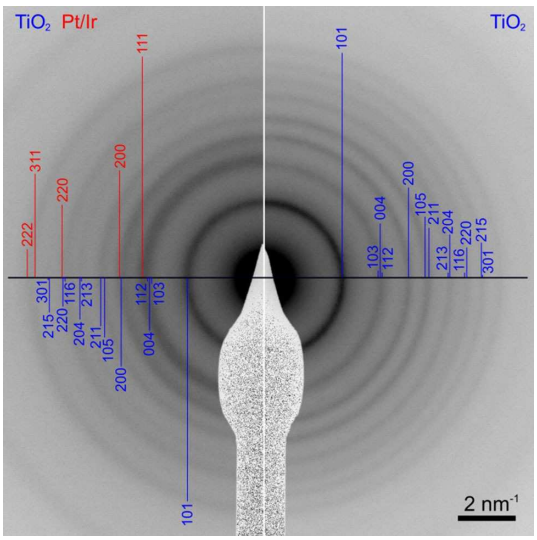


**Figure 4.** Selected-area electron diffraction pattern of a Pt/Ir-coated sample area (left half) and from anodized Ti area only (right half). Blue and red lines indicate the expected power line positions of anatase $TiO_2$ and face-centered cubic Pt/Ir solid solution (see method section). The broad ring pattern indicates the nano-crystalline nature of both Pt/Ir and $TiO_2$.

phases can be distinguished. In SAED, both phases observed in XRD appear, as well, namely, anatase $TiO_2$ and metallic Pt/Ir (Figure 4).

### 2.2. Electrochemical Activity of Coated Ti Felts Towards OER and HER

The electrochemical activity of the coated Ti felts towards oxygen and hydrogen evolution reaction (OER/HER) from water is characterized in acidic media by cyclic voltammetry and steady-state electrolysis. We will compare various total noble metal loadings, various relative amounts of Pt and Ir, and various degrees of mixing. All three parameters can be adjusted by the ALD procedure, that is, by varying the total number of ALD cycles, the relative number of Pt and Ir ALD cycles, and by the exact way in which individual ALD cycles of both materials are combined with each other. In this paper, we will label a sample prepared by x cycles of Pt ALD, then y cycles of Ir ALD, then z−1 repeats of this sequence, as {xPt+yIr}z. In the first step, we will look for a loading that maximizes the mass activity of the electrode for oxygen evolution. In the subsequent step, we will focus on the presence of both noble metals at the particle surface.

Figure 5 demonstrates the effects of anodization and catalyst deposition on the electrochemical behavior of the Ti

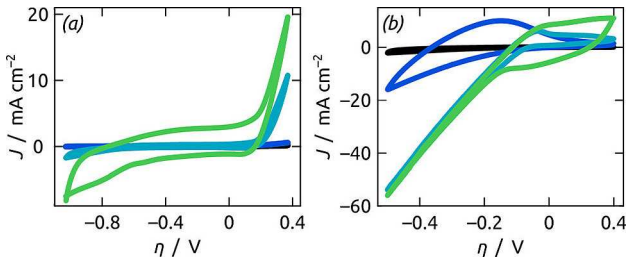


**Figure 5.** Cyclic voltammetry (current density $J$ vs. overpotential $\eta$ at 50 mV s$^{-1}$) on the (a) anodic and (b) cathodic sides recorded in acidic aqueous solution on Ti felts with different features: Ti felt without any treatment (black), anodized Ti felt (dark blue), not anodized Ti felt and coated with catalyst (cyano) and anodized Ti felt and coated with catalyst ({5Pt+5Ir}$_3$, green).

felt. The current at a Ti felt without treatment (black curves) and of an anodized Ti felt (dark blue) remain very low below 1 mA cm$^{-2}$, both on the anodic and cathodic sides. The cyano curve displays a Ti felt not submitted to anodization, coated as {5Pt+5Ir}$_3$. The presence of catalyst causes the appearance of a significant current, both for OER and HER. If the large surface area of an anodized Ti felt is combined with catalyst coated by ALD, a significant hysteretic behavior is observed due to the capacitance increase and the OER current density is almost doubled.

Let us now consider the influence of the catalyst loading of both platinum and iridium on the electrocatalytic activity during steady-state electrolysis. We consider the OER current densities (measured at room temperature) as our main performance parameter (Table 1), whereas we check HER activity, as well, in order to ensure that not only Ir but also Pt is present at the surface and electrocatalytically active (for the bifunctional activity, Table 1).

With a catalyst loading obtained with two individual blocks of 25 Ir ALD cycles followed by 10 Pt cycles, an OER current density of $J=3.5$ mA cm$^{-2}$ is achieved at $\eta=0.27$ V and $J=14.9$ mA cm$^{-2}$ at $\eta=0.47$ V. Current densities towards HER are $J=8.6$ mA cm$^{-2}$ at $\eta=0.20$ V and $J=31.9$ mA cm$^{-2}$ at $\eta=0.40$ V, respectively. Reducing the absolute loading to {3Pt+5Ir} causes a stringent loss of OER current density, even though the last ALD cycles, that is, the most surface-close material, is Ir. The HER current density, however, is hardly affected. The most intimate mixing corresponds to the alternation of individual Pt

**Table 1.** Overview of the current densities in mA cm$^{-2}$ resulting from the oxygen evolution and hydrogen evolution reactions. The data were obtained from steady-state electrolysis at different applied overpotentials in 0.1 M $H_2SO_4$, from 0.17 V to 0.47 V for the OER and from 0.10 V to 0.30 V for the HER.

| | $\eta = 0.17$ V | $\eta = 0.27$ V | $\eta = 0.37$ V | $\eta = 0.47$ V | $\eta = 0.10$ V | $\eta = 0.20$ V | $\eta = 0.30$ V |
|---|---|---|---|---|---|---|---|
| 25Ir + 10Pt | 0.29 | 3.45 | 8.76 | 14.91 | −0.75 | −8.62 | −31.86 |
| 3Pt + 5Ir | 0.02 | 0.05 | 0.24 | 0.33 | −1.12 | −18.17 | −52.40 |
| $\{Pt + Ir\}_2$ | 0.01 | 0.01 | 0.01 | 0.01 | −0.86 | −11.85 | −31.92 |
| $\{2Pt + 2Ir\}_2$ | 0.01 | 0.02 | 0.04 | 0.04 | −1.34 | −15.58 | −52.26 |
| $\{Pt + 4Ir\}_2$ | 0.05 | 0.01 | 0.02 | 0.04 | −0.76 | −6.19 | −20.23 |
| $\{5Pt + 5Ir\}_2$ | 0.02 | 0.60 | 7.30 | 18.18 | −0.91 | −12.52 | −44.15 |
| $\{5Ir + 5Pt\}_3$ | 0.08 | 1.20 | 3.83 | 7.14 | −0.58 | −8.57 | −30.04 |
| $\{5Pt + 5Ir\}_3$ | 0.29 | 5.10 | 16.36 | 26.55 | −4.46 | −18.95 | −58.60 |

and Ir ALD cycles and gives rise to the lowest OER current of all our samples.

This might be related to the lower initial ALD growth rate when compared to the steady-state growth rate.[5,8–9] Indeed, samples with several consecutive cycles of each metal, such as $\{2Pt + 2Ir\}_2$ and $\{1Pt + 4Ir\}_2$, give rise to a modest improvement of OER current. It seems that 5 cycles of each metal is the minimum for obtaining the properties of the bulk: the samples $\{5Pt + 5Ir\}_2$, $\{5Ir + 5Pt\}_3$, and $\{5Pt + 5Ir\}_3$ are very significantly improved. In this case, depositing Ir as the topmost layer is more important for the OER activity than the total amount of material. The effect on HER is visible but less prevalent. The largest OER current density is obtained for the anodized Ti felt with $\{5Pt + 5Ir\}_3$ coating: 5 mA cm$^{-2}$ at $\eta = 0.27$ V and 26 mA cm$^{-2}$ at $\eta = 0.47$ V.

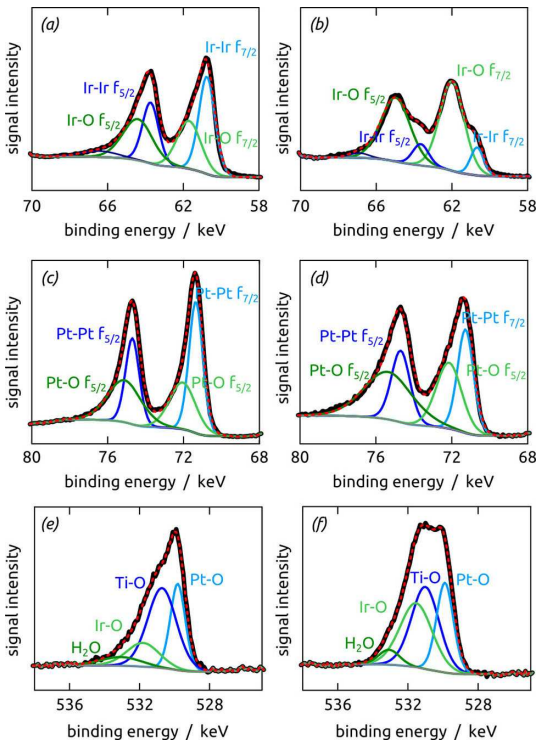


**Figure 6.** X-ray photoelectron spectroscopy on an anodized and coated Ti felt before (a), (c), (e) and after (b), (d), (f) electrochemical treatment. After the electrochemical performance the amount of iridium oxide species increases, whereas platinum remains almost stable.

The surface analysis of our best electrode $\{5Pt + 5Ir\}_3$ by X-ray photoelectron spectroscopy (Figure 6) confirms the presence of both elements on the surface of the solid. Before electrochemistry, both Pt and Ir signals are visible as doublets the deconvolution of which exhibits the presence of both metallic and oxidized element on the surface (Figure 6a,c: metallic Ir 4f at binding energies of 60.8 eV and 63.8 eV,[10] Ir oxide at 62.0 eV and 65.0 eV;[11] metallic/oxide Pt 4f at 71.4 eV and 74.7 eV;[10b,12]). After the sample has been submitted to extended electrolysis, both noble metals display a larger fraction of oxide at the surface, whereby the effect is much more pronounced for Ir than Pt. This corresponds to the established higher oxygen ability of Ir than of Pt.[13] Importantly, both elements are still present at the surface, indicating the stability of our samples to phase separation.

The O 1s region of the XPS spectrum confirms these findings (Figure 6e,f): both Ir and Pt oxides are observable in addition to $TiO_2$ in the as-prepared samples already, but the amount of oxidized Ir increases with respect to the $TiO_2$ internal standard whereas the amount of Pt oxide remains essentially constant. Taken together, the XPS data indicate that within each Pt/Ir particle some segregation occurs upon superficial oxidation of Ir during electrolysis at positive applied potential, but the overall microsctructure of the sample is retained. This is consistent with the stability of the electrochemical response observed over the whole duration of the electrolyses (see Figure S2 and Figure S3 in the Supporting Information).

Let us now convert the current densities to mass activities in order to express how efficiently the noble metal is exploited. An overview of the various catalyst loadings presented for OER and HER in Table 1 is displayed in Figure 7. All values refer to the total loading of both Ir and Pt, determined for each sample via ICP-OES analysis (quantitative optical emission spectroscopic analysis of digested samples injected into an inductively-coupled plasma).

Here again, the optimal OER catalytic activity is found for the $\{5Pt + 5Ir\}_3$ sample. This system yields OER activities of 66 A g$^{-1}$ for an overpotential $\eta = 0.27$ V and 345 A g$^{-1}$ at $\eta = 0.47$ V. For the more facile HER, a catalyst loading of $\{1Pt + 1Ir\}_2$ is already sufficient to achieve 4000 A g$^{-1}$ at $\eta = 0.40$ V.

## 3. Conclusions

A platform has been demonstrated for the systematic optimization of bifunctional Pt/Ir electrocatalysts based on commercial titanium felts. The preparation bases on two major aspects. First, anodization is used to increase the surface area by at least two orders of magnitude. Although the geometric area is by no means exceptionally large, the method yields a controlled geometry in which every surface point is well accessible to the electrolyte. The second important ingredient is the deposition method ALD, with which we are able to tune very finely not only the loading with noble metal catalyst but also its composition and the surface presence of each component. These capabilities enable us to present an optimized system featuring very low noble metal loadings (in the low $\mu g\,cm^{-2}$ range) and record values for mass activity (water oxidation current 345 $A\,g^{-1}$ at $\eta = 0.47$ V). The loadings can be more than an order of magnitude beyond (lower than) the DOE target of $\leq 0.125\ mg\,cm^{-2}$ for 2020 and the mass activity is on the order of the DOE target of $\geq 440\ A\,g^{-1}$.

The absolute current densities achievable with our system at large overpotentials are not exceptionally high.

However, the advantage of the novel platform appears at low overpotential ($\eta < 0.2$ V), where to the best of our knowledge it outperforms all published systems in terms of mass activity (Figure 8). A low-overpotential operation is the most critical performance feature of a regenerative fuel cell, given that it directly determines the round-trip energy storage and release efficiency.

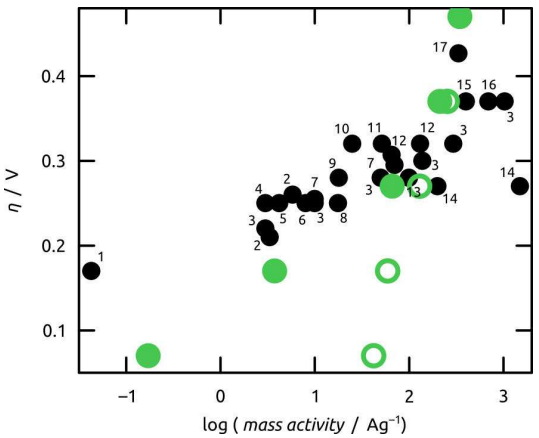


**Figure 8.** Comparison of the oxygen evolution performance (in Tafel plot format) in terms of overpotential $\eta$ and mass activity of our catalyst coated nanostructured electrode (green filled symbols: data obtained from steady-state electrolysis; green empty symbols: data obtained from cyclic voltammetry) with the state of the art (black symbols): 1,[14] 2,[15] 3,[16] 4,[17] 5,[18] 6,[19] 7,[20] 8,[21] 9,[22] 10,[23] 11,[24] 12,[25] 13,[26] 14,[27] 15,[28] 16,[29] 17.[30]

## Experimental Section

### Materials

Standard chemicals were purchased from Sigma Aldrich, VWR and STREM and used without further purification. Ti felts (article ST/Ti/20/350/50) were obtained from Bekaert: they have a thickness of 160 μm, the fibers have a diameter of 20 μm and the mean pore size is 40 μm.

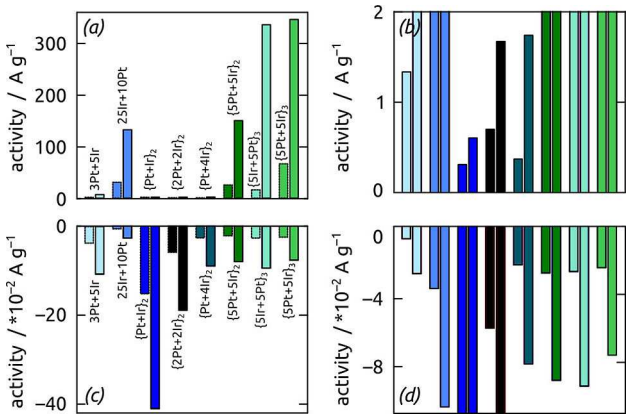


**Figure 7.** Activity plots calculated per gramm of total catalyst loading for both oxygen evolution reaction and hydrogen evolution reaction for $\eta = 0.27$ V and $\eta = 0.47$ V or $\eta = 0.20$ V and $\eta = 0.40$ V, respectively. For OER the sample with a catalyst loading of $\{5Pt + 5Ir\}_3$ shows the highest activity. For HER already a catalyst loading of $\{Pt + Ir\}_2$ is enough for a very efficient catalytic activity.

### Preparation of Electrodes

The Ti felts were anodized in glycerol and $NH_4F$ (0.5 wt.%) under an applied potential of +40 V for 2 h using a graphite foil as counter electrode. After washing the Ti felts with ethanol and water, ALD coating was performed in a commercial Gemstar-6 ALD reactor from Arradiance. Ethylcyclopentadienyl-1,3-cyclohexadiene-iridium (I) ((EtCp)Ir(CHD) from Strem), trimethyl-(methyl¬cyclo-penta¬dienyl)¬platinum ($MeCpPtMe_3$) and ozone were used as precursors. Ozone was produced from oxygen in an ozone generator model BMT 803N. The Ir-precursor and Pt-precursor were heated to 90 °C and to 50 °C, respectively, whereas the chamber temperature was set to 220 °C.

### Characterization

The geometry and morphology of Ti felts before and after ALD coatings were investigated using a Scanning Electron Microscope JEOL JSM 6400 equipped with a $LaB_6$ cathode and an EDX detector from SAMx.

One of the samples $\{5Pt + 5Ir\}_3$ was chosen for structural and elemental analysis at high spatial resolution by means of (Scanning) Transmission Electron Microscopy ((S)TEM). Cross-section TEM specimen (i.e., with surface normal of the TEM lamella parallel to the axis of the Ti wires) was prepared by standard lift-out technique using a ThermoFischer Helios Nanolab 660 dual beam focused ion beam (FIB)/SEM. STEM/TEM studies were performed with a (ThermoFischer) Titan³ Themis microscope operated at 200 kV. The microscope is equipped with an ultra-bright X-FEG electron source, spherical aberration correctors in both probe-forming side and imaging side. EDX elemental maps were acquired using the Super-X detector array and a high probe current. Care was taken so that the intense electron beam did not damage/alter the structure of the sample. The raw data and the spectrum images were evaluated using the Velox software. Selection area electron diffraction (SAED) was acquired with parallel beam and an aperture covered area of about 200 nm in diameter. The experimental and theoretical power

pattern/line is evaluated with the JEMS software. The crystal structure of Pt/Ir is assumed to be solid solution of Pt and Ir in face-centered cubic structure and the lattice parameter is assumed to be the average of pure Pt and Ir.

The loading of the Pt/Ir catalyst was determined by inductively coupled plasma optical emission spectrometry (ICP-OES, Optima 8300, Perkin Elmer). For the ICP-OES analysis 4-point calibrations (50, 10, 1 and 0.1 ppm) were performed by diluting certified standards. Samples were measured in triplicate and mean value with the standard deviation are reported. The crystal structure was analyzed by X-ray diffraction in Bragg-Brentano geometry using a Bruker D8 Advance equipped with a Cu Kα source and LynxEye XE–T detector.

### Electrochemical Investigation

All electrochemical measurements were performed in a three-electrode setup with an Ag/AgCl reference electrode (Bioanalytical Systems, Inc.) with a standard redox potential of +0.20 V versus NHE and a graphite counter electrode. Cyclic voltammetry and steady-state electrolysis were recorded in aqueous $H_2SO_4$ (0.1 M) using a Gamry Interface 1000 potentiostat. CVs were recorded at 50 mV $s^{-1}$ starting at the open circuit potential between 0.0 V and +1.4 V for the oxygen evolution reaction (vs. Ag/AgCl). The applied potential for steady-state electrolyses were varied between +1.1 V and +1.5 V and −0.3 V and −0.6 V, respectively (overpotentials $\eta$ = 0.07 V to 0.47 V and $\eta$ = 0.10 to 0.40 V). A test performed in 0.1 M NaOH confirms that the sample is also active in alkaline media (Figure S4).

## Acknowledgements

*This research was funded by the German Ministry of Education and Research (BMBF) in the project 'TubulAir±'A (project number 03SF0436G), the European Research Council with an ERC Consolidator Grant (grant number 647281, 'Solacylin'), and by the German Research Foundation (DFG) via the Excellence Cluster "Engineering of Advanced Materials" (EXC315) bridge funding. We thank Dr. A. Both-Engel for XPS measurements.*

## Conflict of Interest

The authors declare no conflict of interest.

**Keywords:** catalysis · electrodes · fuel cells · materials science · metals

[1] J. Noack, N. Roznyatovskaya, T. Herr, P. Fischer, *Angew. Chem. Int. Ed.* **2015**, *54*, 9776.
[2] Y. Wang, D. Y. C. Leung, J. Xuan, H. Wang, *Renewable Sustainable Energy Rev.* **2017**, *75*, 775.
[3] a) S. S. Hosseiny, M. Saakes, M. Wessling, *Electrochem. Commun.* **2011**, *13*, 751; b) F. Rahman, M. Skyllas-Kazacos, *J. Power Sources* **2009**, *189*, 1212; c) S. Ressel, A. Laube, S. Fischer, A. Chica, T. Flower, T. Struckmann, *J. Power Sources* **2017**, *355*, 199; d) M. Skyllas-Kazacos, M. Rychcik, R. G. Robins, A. G. Fane, M. A. Green, *J. Electrochem. Soc.* **1986**, *133*, 1057.
[4] a) M. G. Chourashiya, A. Urakawa, *J. Mater. Chem. A* **2017**, *5*, 4774; b) J. Pettersson, B. Ramsey, D. Harrison, *J. Power Sources* **2006**, *157*, 28; c) E. Rasten, G. Hagen, R. Tunold, *Electrochim. Acta* **2003**, *48*, 3945.
[5] L. Assaud, J. Schumacher, A. Tafel, S. Bochmann, S. Christiansen, J. Bachmann, *J. Mater. Chem. A* **2015**, *3*, 8450.
[6] a) S. Schlicht, S. Haschke, V. Mikhailovskii, A. Manshina, J. Bachmann, *ChemElectroChem* **2018**, *5*, 1259; b) T. Aaltonen, M. Ritala, T. Sajavaara, J. Keinonen, M. Leskelae, *Chem. Mater.* **2003**, *15*, 1924.
[7] J. Bachmann, *Beilstein J. Nanotechnol.* **2014**, *5*, 245.
[8] J. Dendooven, R. K. Ramachandran, K. Devloo-Casier, G. Rampelberg, M. Filez, H. Poelman, G. B. Marin, E. Fonda, C. Detavernier, *J. Phys. Chem. C* **2013**, *117*, 20557.
[9] L. Baker, A. Cavanagh, D. Seghete, S. M. George, A. J. M. Mackus, W. M. M. Kessels, Z. Y. Liu, F. T. Wagner, *J. Appl. Phys.* **2011**, *109*, 084333.
[10] a) N. V. Gel'fond, I. K. Igumenov, A. I. Boronin, V. I. Bukhtiyarov, M. Y. Smirnov, I. P. Prosvirin, R. I. Kvon, *Surf. Sci.* **1992**, *275*, 323; b) J. F. Moulder, J. Chastain, *Handbook of X-ray Photoelectron Spectroscopy: A Reference Book of Standard Spectra for Identification and Interpretation of XPS Data*, Physical Electronics Division, Perkin-Elmer Corporation, **1992**.
[11] a) V. Pfeifer, T. E. Jones, J. J. Velasco Velez, C. Massue, M. T. Greiner, R. Arrigo, D. Teschner, F. Girgsdies, M. Scherzer, J. Allan, M. Hashagen, G. Weinberg, S. Piccinin, M. Haevecker, A. Knop-Gericke, R. Schloegl, *Phys. Chem. Chem. Phys.* **2016**, *18*, 2292; b) R. D. L. Smith, B. Sporinova, R. D. Fagan, S. Trudel, C. P. Berlinguette, *Chem. Mater.* **2014**, *26*, 1654.
[12] a) A. S. Aricò, A. K. Shukla, H. Kim, S. Park, M. Min, V. Antonucci, *Appl. Surf. Sci.* **2001**, *172*, 33; b) Q. Cai, W. Hong, J. Li, C. Jian, W. Liu, *RSC Adv.* **2017**, *7*, 21809; c) E. I. Vovk, A. V. Kalinkin, M. Y. Smirnov, I. O. Klembovskii, V. I. Bukhtiyarov, *J. Phys. Chem. C* **2017**, *121*, 17297.
[13] a) S. M. Alia, B. Rasimick, C. Ngo, K. C. Neyerlin, S. S. Kocha, S. Pylypenko, H. Xu, B. S. Pivovar, *J. Electrochem. Soc.* **2016**, *163*, F3105; b) R. Koetz, H. Neff, S. Stucki, *J. Electrochem. Soc.* **1984**, *131*, 72; c) D. J. Miller, H. Öberg, S. Kaya, H. Sanchez Casalongue, D. Friebel, T. Anniyev, H. Ogasawara, H. Bluhm, L. G. M. Pettersson, A. Nilsson, *Phys. Rev. Lett.* **2011**, *107*, 195502; d) M. J. N. Pourbaix, J. Van Muylder, N. de Zoubov, *Platinum Met. Rev.* **1959**, *3*, 47; e) N. Roy, Y. Sohn, K. T. Leung, D. Pradhan, *J. Phys. Chem. C* **2014**, *118*, 29499.
[14] N. Mamaca, E. Mayousse, S. Arrii-Clacens, T. W. Napporn, K. Servat, N. Guillet, K. B. Kokoh, *Appl. Catal. B* **2012**, *111–112*, 376.
[15] S. Song, H. Zhang, X. Ma, Z. Shao, R. T. Baker, B. Yi, *Int. J. Hydrogen Energy* **2008**, *33*, 4955.
[16] S. M. Alia, S. Shulda, C. Ngo, S. Pylypenko, B. S. Pivovar, *ACS Catal.* **2018**, *8*, 2111.
[17] Y. Lee, J. Suntivich, K. J. May, E. E. Perry, Y. Shao-Horn, *J. Phys. Chem. Lett.* **2012**, *3*, 399.
[18] Z. Ma, Y. Zhang, S. Liu, W. Xu, L. Wu, Y.-C. Hsieh, P. Liu, Y. Zhu, K. Sasaki, J. N. Renner, K. E. Ayers, R. R. Adzic, J. X. Wang, *J. Electroanal. Chem.* **2018**, *819*, 296.
[19] P. Lettenmeier, L. Wang, U. Golla-Schindler, P. Gazdzicki, N. A. Canas, M. Handl, R. Hiesgen, S. S. Hosseiny, A. S. Gago, K. A. Friedrich, *Angew. Chem. Int. Ed.* **2016**, *55*, 742.
[20] E. Oakton, D. Lebedev, M. Povia, D. F. Abbott, E. Fabbri, A. Fedorov, M. Nachtegaal, C. Coperet, T. J. Schmidt, *ACS Catal.* **2017**, *7*, 2346.
[21] T. Zhang, S.-C. Li, W. Zhu, Z.-P. Zhang, J. Gu, Y.-W. Zhang, *Nanoscale* **2017**, *9*, 1154.
[22] D. F. Abbott, D. Lebedev, K. Waltar, M. Povia, M. Nachtegaal, E. Fabbri, C. Coperet, T. J. Schmidt, *Chem. Mater.* **2016**, *28*, 6591.
[23] G. C. da Silva, M. R. Fernandes, E. A. Ticianelli, *ACS Catal.* **2018**, *8*, 2081.
[24] J. Lim, D. Park, S. S. Jeon, C.-W. Roh, J. Choi, D. Yoon, M. Park, H. Jung, H. Lee, *Adv. Funct. Mater.* **2018**, *28*, n/a.
[25] B. M. Tackett, W. Sheng, S. Kattel, S. Yao, B. Yan, K. A. Kuttiyiel, Q. Wu, J. G. Chen, *ACS Catal.* **2018**, *8*, 2615.
[26] P. Lettenmeier, J. Majchel, L. Wang, A. S. Gago, K. A. Friedrich, V. A. Saveleva, S. Zafeiratos, E. R. Savinova, J. J. Gallet, F. Bournel, J. J. Gallet, F. Bournel, K. A. Friedrich, *Chem. Sci.* **2018**, *9*, 3570.
[27] E. Slavcheva, I. Radev, S. Bliznakov, G. Topalov, P. Andreev, E. Budevski, *Electrochim. Acta* **2007**, *52*, 3889.
[28] K. E. Ayers, J. N. Renner, N. Danilovic, J. X. Wang, Y. Zhang, R. Maric, H. Yu, *Catal. Today* **2016**, *262*, 121.
[29] H.-S. Oh, H. N. Nong, T. Reier, M. Gliech, P. Strasser, *Chem. Sci.* **2015**, *6*, 3321.
[30] Y. Shi, Z. Lu, L. Guo, Z. Wang, C. Guo, H. Tan, C. Yan, *Int. J. Hydrogen Energy* **2018**, *43*, 9133.

Manuscript received: August 31, 2018
Accepted manuscript online: September 26, 2018
Version of record online: October 23, 2018